Monthly Notices
of the
ROYAL ASTRONOMICAL SOCIETY

MNRAS **464,** 1771–1782 (2017)
Advance Access publication 2016 September 8

doi:10.1093/mnras/stw2263

Feeding versus feedback in active galactic nuclei from near-infrared integral field spectroscopy – XII. NGC 5548

Astor J. Schönell, Jr,[1]★ Thaisa Storchi-Bergmann,[1] Rogemar A. Riffel[2]★ and Rogério Riffel[1]

[1]*Instituto de Física, Universidade Federal do Rio Grande do Sul, Av. Bento Goncalves 9500, 91501-970 Porto Alegre, RS, Brazil*
[2]*Universidade Federal de Santa Maria, Departamento de Física, Centro de Ciências Naturais e Exatas, 97105-900 Santa Maria, RS, Brazil*

Accepted 2016 September 7. Received 2016 September 5; in original form 2016 June 1

ABSTRACT

We map the gas excitation and kinematics, and the stellar population properties of the Seyfert 1 galaxy NGC 5548 using Gemini Near Infrared Integral Field Spectrograph in the *J* and *K* bands at a spatial and velocity resolution of 105 pc and 45 km s^{-1}, respectively. Emission-line flux distributions in ionized and molecular gas extend up to ≈400 pc from the nucleus, where they are found to peak. The mass of H II is 4.8±0.6 × 10^6 M$_\odot$ and the mass of warm H_2 is 1.1±0.2 × 10^3 M$_\odot$, while the mass of cold H_2 is estimated as 5.8±1.2 × 10^8 M$_\odot$. The Pa β emission shows two kinematic components: one in blueshift, with velocity reaching ≈−300 km s^{-1} and another showing a velocity field characteristic of rotation in the galaxy plane. The blueshifted component is also observed in the coronal line [S IX]λ1.2523 μm, while the rotational component is also observed in the molecular gas. We interpret this velocity field as due to gas rotating in the galaxy plane plus an outflow, and estimate a mass outflow rate of 6.8±0.75 M$_\odot$ yr^{-1}. Spectral synthesis of the continuum shows nuclear emission dominated by a featureless AGN continuum combined with hot dust emission attributed to a dusty torus. The stellar population is dominated by an old (2 Gyr < t ≤ 15 Gyr) component between 160 and 300 pc, while closer to the nucleus, an intermediate age (50 Myr < t ≤ 2 Gyr) component contributes at levels ranging from ≈40 per cent to ≈100 per cent to the flux at 2.12 μm.

Key words: galaxies: active – galaxies: individual: NGC 5548 – galaxies: kinematics and dynamics – galaxies: nuclei – galaxies: Seyfert.

1 INTRODUCTION

The study of the narrow-line region of nearby active galactic nuclei (AGN) allows the mapping of the processes of feeding of a nuclear supermassive black hole – via gas inflows (e.g. Fathi et al. 2006; Storchi-Bergmann et al. 2007; Davies et al. 2009; Müller Sánchez et al. 2009; Schnorr Müller et al. 2011) and its feedback – via the interaction of the AGN radiation and outflows with the circumnuclear gas, affecting its kinematics and excitation (Wilson et al. 1993; Schmitt & Kinney 1996; Veilleux, Goodrich & Wilson 1997; Ferruit, Wilson & Mulchaey 2000; Veilleux, Cecil & Bland-Hawthorn 2005; Holt et al. 2006; Crenshaw & Kraemer 2007; Crenshaw et al. 2009, 2010; Fischer et al. 2010; Müller-Sánchez et al. 2011).

Our group, AGN integral field spectroscopy, has been mapping the feeding and feedback processes in nearby AGN using near-infrared (NIR) integral field spectroscopic observations mostly with the instrument Near Infrared Integral Field Spectrograph (NIFS) at the Gemini North Telescope. Studies in the NIR have the advantage of being less affected by dust obscuration, allowing also the observation of the properties of the molecular gas.

The main findings of our group so far have been that the molecular gas- traced by *K*-band H_2 emission, and the ionized gas traced by H I recombination lines and [Fe II] emission, present distinct flux distributions and kinematics. Usually, the H_2 emitting gas is restricted to the plane of the galaxy, while the ionized gas extends also to high latitudes and is associated with the radio emission, when present (Riffel et al. 2006, 2008, 2009a, 2011b; Storchi-Bergmann et al. 2009, 2010; Riffel, Storchi-Bergmann & Nagar 2010a). The kinematics of the ionized gas, and in particular of the [Fe II] emitting gas shows, in many cases (but not always), a strong outflowing component associated with radio jets from the AGN, while the H_2 kinematics is usually dominated by rotation, including streaming motions towards the nucleus. Davies et al. (2009), using the instrument SINFONI (Spectrograph for Integral Field Observations in the Near Infrared) at the Very Large Telescope, found similar results – molecular gas inflows towards the nucleus of NGC 1097, while

★ E-mail: juniorfisicoo@gmail.com (AJS); rogemar@ufsm.br (RAR)

Müller Sánchez et al. (2009) mapped similar inflows feeding and obscuring the active nucleus of NGC 1068. Müller-Sánchez et al. (2011) mapped outflows in ionized gas around seven AGN, and Davies et al. (2014) analysed molecular and ionized gas inflows and outflows in five active galaxies, both also using SINFONI.

In this study, we present the gaseous distribution, excitation, kinematics, and stellar population (SP) distribution of the inner ≈500 pc radius of the Seyfert 1.5 galaxy NGC 5548 (Mrk 1509), a spiral galaxy (S0/a) at a distance of 79.1 Mpc, where 1.0 arcsec corresponds to 384 parsecs at the galaxy.

This paper is organized as follows: in Section 2, we describe the observations and data reduction procedures. The results are presented in Section 3 and discussed in Section 4. We present our conclusions in Section 5.

2 OBSERVATIONS AND DATA REDUCTION

Observations of the inner region of NGC 5548 were obtained with the instrument NIFS (McGregor et al. 2003) using the Gemini North Adaptive Optics system ALTAIR, in 2012 July under the programme GN-2012A-Q-57. The exposures followed the standard Sky-Object-Object-Sky dither sequence and were obtained in the *J* band using the J_G5603 grating and ZJ_G0601 filter, and in the K_l band using the Kl_G5607 grating and HK_G0603 filter.

On-source and sky position observations were both obtained with individual exposure times of 450 s. Two sets of observations were obtained: the first, in the *J* band, was centred at 1.25 μm and covered the spectral range 1.14–1.36 μm, and the second, in the K_l band, was centred at 2.3 μm and covered the spectral range 2.10–2.53 μm. The total on source exposure was 90 min (45 min in each band).

The data reduction procedure included trimming of the images, flat-fielding, sky subtraction, wavelength and spatial distortion calibrations. We also removed the telluric bands and flux calibrated the frames by interpolating a blackbody function to the spectrum of the telluric standard star. These procedures were executed using tasks contained in the NIFS software package which is part of GEMINI IRAF package, as well as generic IRAF tasks.

The final integral field unit (IFU) data cube for each band contains ≈4000 spectra, with each spectrum corresponding to an angular coverage of 0.05 arcsec × 0.05 arcsec, which translates into ≈20 × 20 pc^2 at the galaxy and covering the inner 3.0 arcsec × 3.0 arcsec (≈1.1 × 1.1 kpc^2) of the galaxy.

We have replaced each spatial pixel by the median of its value and that of its first eight neighbours as well as we used the Butterworth filter (Riffel et al. 2016) to increase the signal-to-noise (S/N) ratio and allow the fitting of the emission-line profiles. The full width at half-maximum (FWHM) of the arc lamp lines in the *J* band is 1.65 Å, corresponding in velocity space to 40 km s^{-1}, while in the K_l band the FWHM of the arc lamp lines is 3.45Å, corresponding to 45 km s^{-1}. The angular resolution in *J* band obtained from the FWHM of the spatial profile of the flux distribution of the broad component of the Pa β is 0.28 arcsec corresponding to 105 pc at the galaxy. The spatial resolution in the K_l band is 0.2 arcsec, corresponding to 75 pc at the galaxy and was obtained from the profile of the nuclear source which is dominated by the contribution of the unresolved AGN.

3 RESULTS

In the top-left panel of Fig. 1, we show a *z*-band image of NGC 5548 obtained from the SDSS (Sloan Digital Sky Survey; Baillard et al. 2011). In the top-right panel, we present an optical image of NGC 5548 obtained with *HST* (*Hubble Space Telescope*) through the filter *F*606*W* (Malkan, Gorjian & Tam 1998). In the bottom panels, we display in the left a *J*-band continuum image constructed by collapsing the spectra within a 100 Å window centred at 1.23 μm, and in the right a *K*-band continuum image centred at 2.22 μm. In Fig. 2, we present two IFU spectra integrated within 0.25 arcsec × 0.25 arcsec aperture. One of them is at the nucleus and the other at 0.4 arcsec south-east of it (position A), which was randomly chosen just to present a characteristic extranuclear spectrum. The nucleus was defined to be the location of the peak of the continuum.

3.1 Emission-line flux distributions

In order to map the flux distributions as well as the centroid velocity and velocity dispersion of the emission lines observed in the *J* and *K* bands ([P II]λ1.1886 μm, [S IX]λ1.2523 μm, [Fe II]λ1.2570 μm, Pa βλ1.2822 μm and H_2λ2.1218 μm), we have used the PROFIT routine (Riffel 2010) to fit the profiles at each pixel over the whole field-of-view. The integrated flux, centroid velocity and velocity dispersion values were obtained by the fit of the emission-line profiles using both Gaussian and Gauss–Hermite (GH) series. The Pa β emission line needed to be fitted with a broad component and this was made using a modified PROFIT routine in three steps: (i) fit two Gaussians to the broad component; (ii) subtract it from the spectra where it is present, and (iii) fit the narrow component.

The narrow component of Pa β emission-line profile was also fitted with two Gaussians because at many locations it shows two peaks. In Fig. 3, we show the fits of the broad and narrow components for the central pixel (peak of the continuum in *J* band) to demonstrate the need of a two-component fit for Pa β. The remaining lines were fitted with a single component of GH series. We do not show the GH moments h_3 and h_4 because they are very noisy, not adding relevant information.

In Fig. 4, we present the flux distribution maps for all the lines fitted. We have masked out the bad fits (using the relative χ^2 parameter of the fit, which is an output from the PROFIT routine) and regions with S/N ratio lower than 3. All maps have their peak fluxes at the same position, which coincides with the peak of the continuum and is adopted as the position of the nucleus.

The [P II]λ1.1886 μm and [S IX]λ1.2523 μm flux distributions are very compact, reaching ≈0.4 arcsec from the nucleus in all directions. The flux distribution of these two coronal lines are thus barely resolved, extending to ≈150 pc from the nucleus, which is typical for coronal lines (e.g. Rodríguez-Ardila et al. 2006; Mazzalay, Rodríguez-Ardila & Komossa 2010; Riffel et al. 2011b; Schönell et al. 2014). The [Fe II]λ1.2570 μm flux distribution is more extended than the coronal lines, reaching almost 0.6 arcsec (230 pc) in all directions.

The blue component of Pa β is extended in all directions up to ≈0.8 arcsec (≈300 pc) (region with S/N ≥ 3) and is the brightest among the observed lines.

We have concluded that the Pa β has two components only within 0.8 arcsec (≈300 pc) from the nucleus. Beyond this region, a good fit is obtained with a single GH component. Therefore, we combined the fluxes of the red component from the inner region with the single GH component from the surrounding region, which extents up to ≈1.2 arcsec (≈500 pc) from the nucleus.

The H_2 line is the only K_l band line that we were able to fit due to the low S/N ratio (S/N < 3) of the other lines present there. The H_2 flux is extended in all directions reaching ≈0.6 arcsec (≈230) from the nucleus.

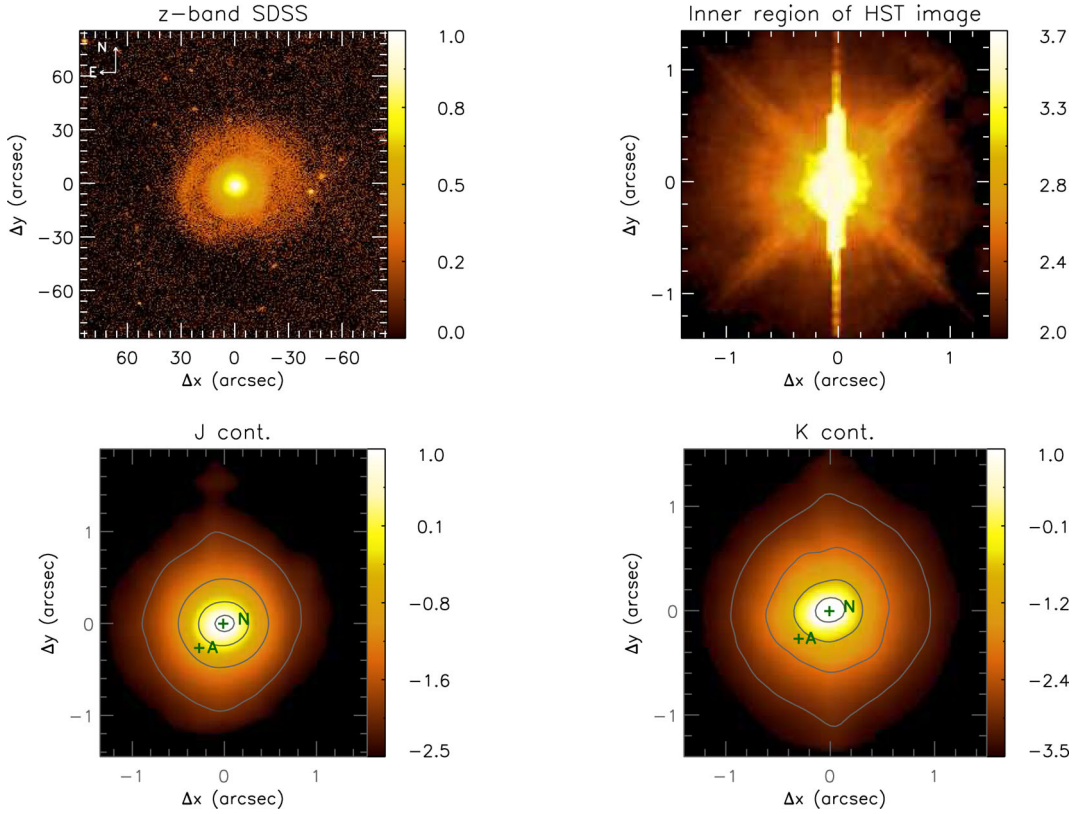

Figure 1. Images of NGC 5548. Top-left panel: SDSS z-band image centred at 8932 Å (Baillard et al. 2011) in arbitrary flux units. Top-right panel: *HST* optical image obtained through the filter *F606W* (Malkan et al. 1998). Botton-left panel: 1.23 μm continuum image obtained from the NIFS data cube with fluxes shown in logarithmic units of 10^{-17} erg s^{-1} cm^2. Bottom-Right panel: 2.22 μm continuum image obtained from the NIFS data cube with fluxes shown in logarithmic units of 10^{-17} erg s^{-1} cm^2.The label N marks the position of the continuum peak and the label A marks the extranuclear position where the spectra of Fig. 2 was obtained.

3.2 Gas kinematics

The PROFIT routine (Riffel 2010) also provides the centroid velocity (v), velocity dispersion (σ) and higher order GH moments (h_3 and h_4), that can be used to map the gas kinematics. In Fig. 5, we present the centroid velocity fields after subtraction of the heliocentric systemic velocity of 5160 ± 10 km s^{-1}, which was obtained through a model fitted to the H_2 velocity field and will be discussed in the next section. The white regions in the figures represent locations where the S/N ratio was too low for a reliable fit.

In Fig. 5 we can see the [P II] velocity field with low centroid velocities, most of them close to zero reaching no more than ≈60 km s^{-1}. The [S IX] velocity field is entirely blueshifted, reaching up to −250 km s^{-1} in most regions. The [Fe II] velocity field is similar to that of [P II]. The Pa β velocity field for the blue component shows velocities in the range −250 to −100 km s^{-1}, while the red component shows a rotation pattern, with blueshifts to the south-east and redshifts to the north-west. The H_2 velocity field also presents a rotation pattern, similar to that of the red component of Pa β.

Fig. 6 shows the velocity dispersion maps for the same lines as for the velocity fields. The σ map for the [P II] shows most values close to ≈100 km s^{-1}, reaching ≈130 km s^{-1} to the west, while the [S IX] σ map is noisier showing values close to 200 km s^{-1}. The [Fe II] σ map has values ranging from ≈50 to ≈125 km s^{-1} with the higher values closer to the nucleus. The blue component of Pa β shows an increase in the σ values around the nucleus of up to 200 km s^{-1} just to the south of the nucleus (≈0.3 arcsec – 105 pc). The red component of Pa β shows lower values of σ, in the range 50–120 km s^{-1}). The H_2 map shows lower values of σ, in the range 50–100 km s^{-1}.

3.3 Channel maps

We have constructed channel maps along the emission-line profiles, but as most emission lines are barely resolved and do not have much kinematic information, we show only the $H_2\lambda2.1218$ μm channel maps in Fig. 7. The panels in the figure show the flux in logarithmic units integrated in velocity bins centred at the velocity shown in the top-left corner of each panel (relative to the systemic velocity of the galaxy). The central cross marks the position of the nucleus. The velocity bins are 30 km s^{-1} (corresponding to 1 spectral pixel) for all panels except the first and last panels, integrated in bins of 100 km s^{-1} (corresponding to 3 spectral pixels). The maps show blueshifts of up to −143 km s^{-1} to the south-east and redshifts of up to 128 km s^{-1} to the north-west. For velocities close to zero the flux distribution is more compact, reaching only 0.6 arcsec (230 pc) with no preferential direction.

3.4 Stellar population synthesis

In this subsection, for the first time, we map the SP properties within the inner 1.5 arcsec (≈600 pc) at a spatial resolution of ≈105 pc of a Seyfert 1 galaxy NGC 5548 derived from the NIR spectra. In order to do this, we simultaneously fit the stellar continuum of the

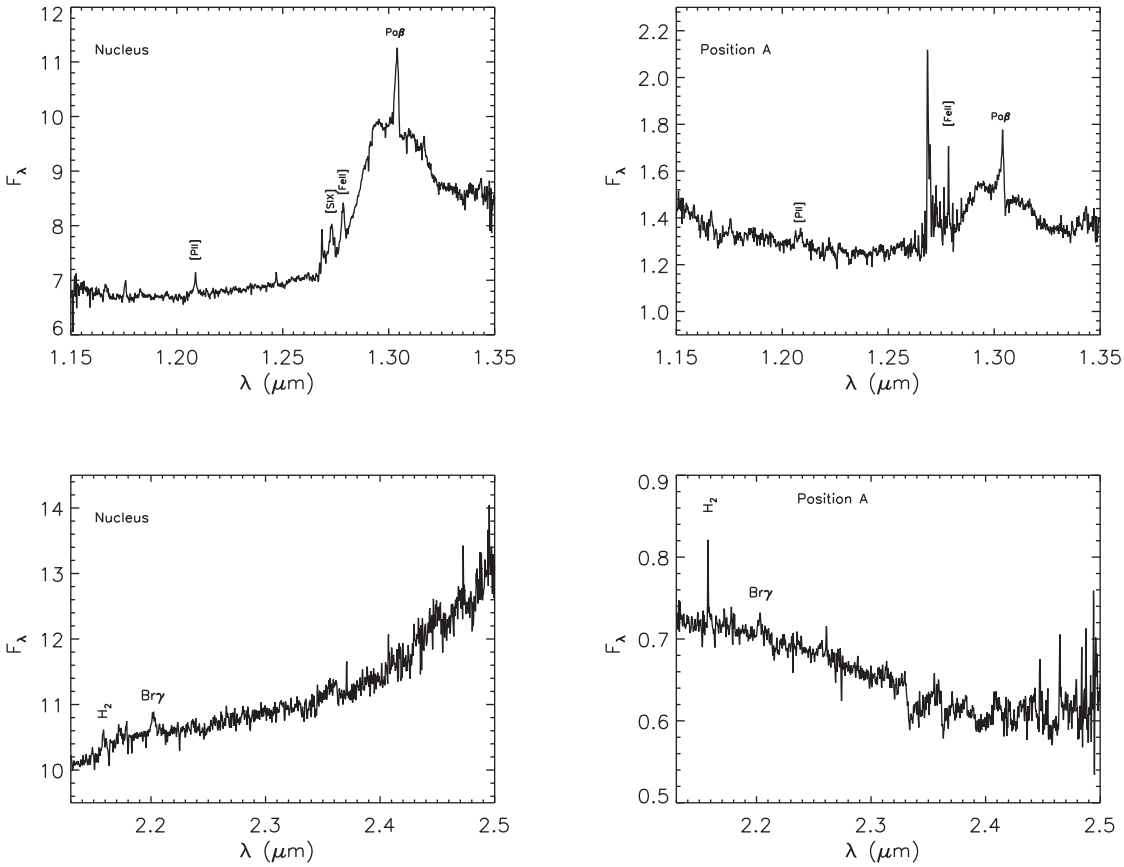

Figure 2. Spectra obtained with an aperture of 0.25 arcsec × 0.25 arcsec centred at the nucleus and at 0.4 arcsec south-east from it (position A, marked in Fig. 1). Flux units: 10^{-17} erg s^{-1} cm^{-2} Å^{-1}.

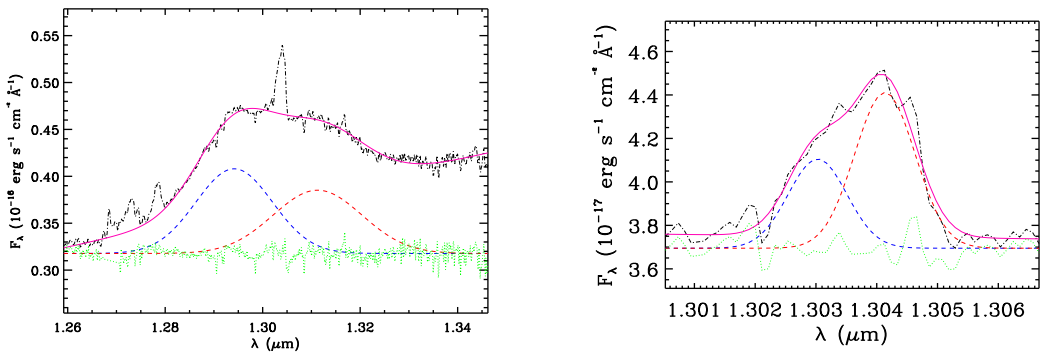

Figure 3. Left-hand panel: fit of the broad Pa β component with two Gaussians. Right-hand panel: fit of the narrow component also with two Gaussians.

J and *K* bands applying the method described in Riffel et al. (2009b) as follows.

Using the STARLIGHT code (Cid Fernandes et al. 2004, 2005, 2009; Asari et al. 2007; Mateus et al. 2011), we performed the SP synthesis. The code uses computational techniques originally developed for semi-empirical population synthesis with ingredients from evolutionary synthesis models (Cid Fernandes et al. 2004, 2005) to fit the whole spectrum, excluding emission lines and spurious data. To summarize, an observed spectrum (O_λ) is fitted with a combination, in different proportions, of N_* simple stellar populations (SSPs). Maraston (2005) provides the evolutionary population synthesis (EPS) models used here. The extinction of the SSPs is parametrized by the v-band extinction A_v and modelled by STARLIGHT as due to foreground dust, and the extinction law used was Cardelli, Clayton & Mathis (1989). The code solves the following equation to model a spectrum M_λ:

$$M_\lambda = M_{\lambda 0} \sum_{j=1}^{N_*} x_j b_{j,\lambda} r_\lambda \bigotimes G(v_*, \sigma_*), \quad (1)$$

where x is the population vector, whose components x_j ($j = 1,..., N_*$) represent the fractional contribution of each SSP in the base to the total synthetic flux at λ_0. The spectrum of the jth SSP of the base of elements normalized at λ_0 is represented by $b_{j,\lambda}$, the reddening term is given by $r_\lambda = 10^{-0.4(A_\lambda - A_{\lambda 0})}$, $M_{\lambda 0}$ is the synthetic flux at the normalization wavelength, $\bigotimes$ represents the convolution operator and $G(v_*, \sigma_*)$ gives the Gaussian distribution used to model the line-of-sight stellar motions, that has a dispersion σ_*, centred at a

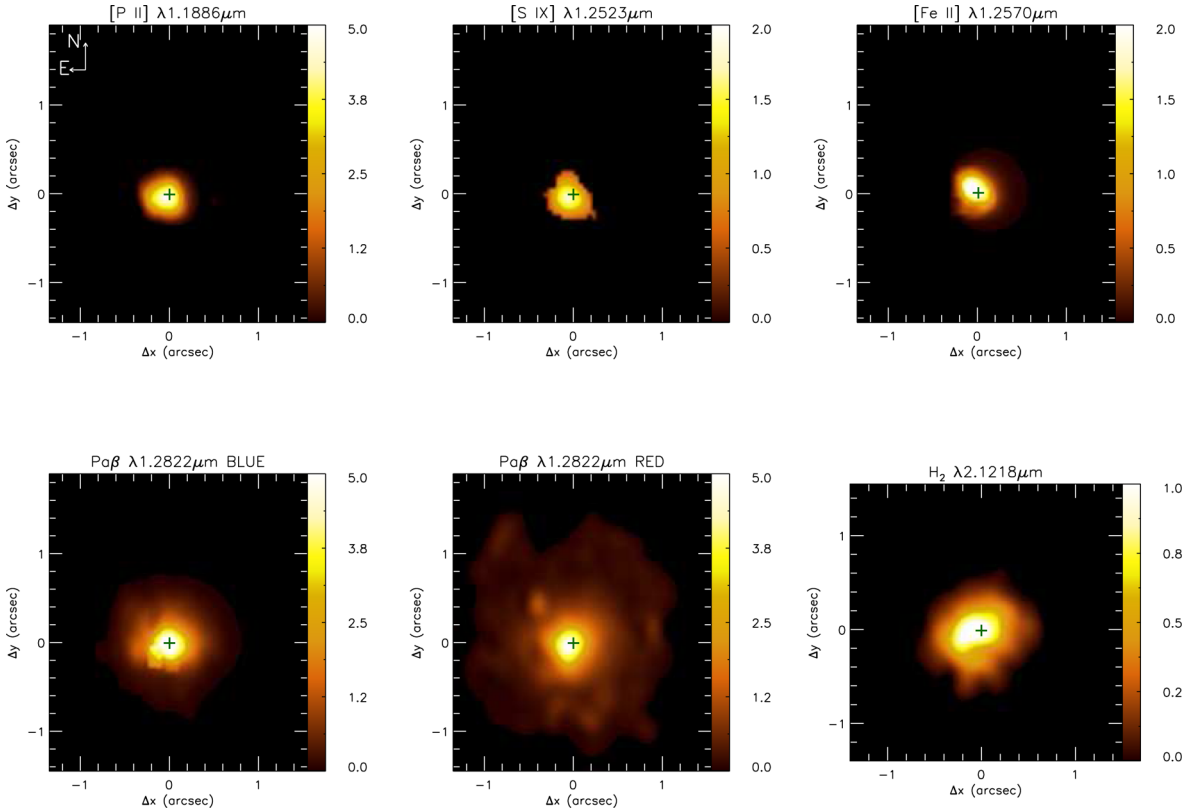

Figure 4. Emission-line flux distributions. The flux units are 10^{-17} erg s^{-1} cm^{-2} Å^{-1}.

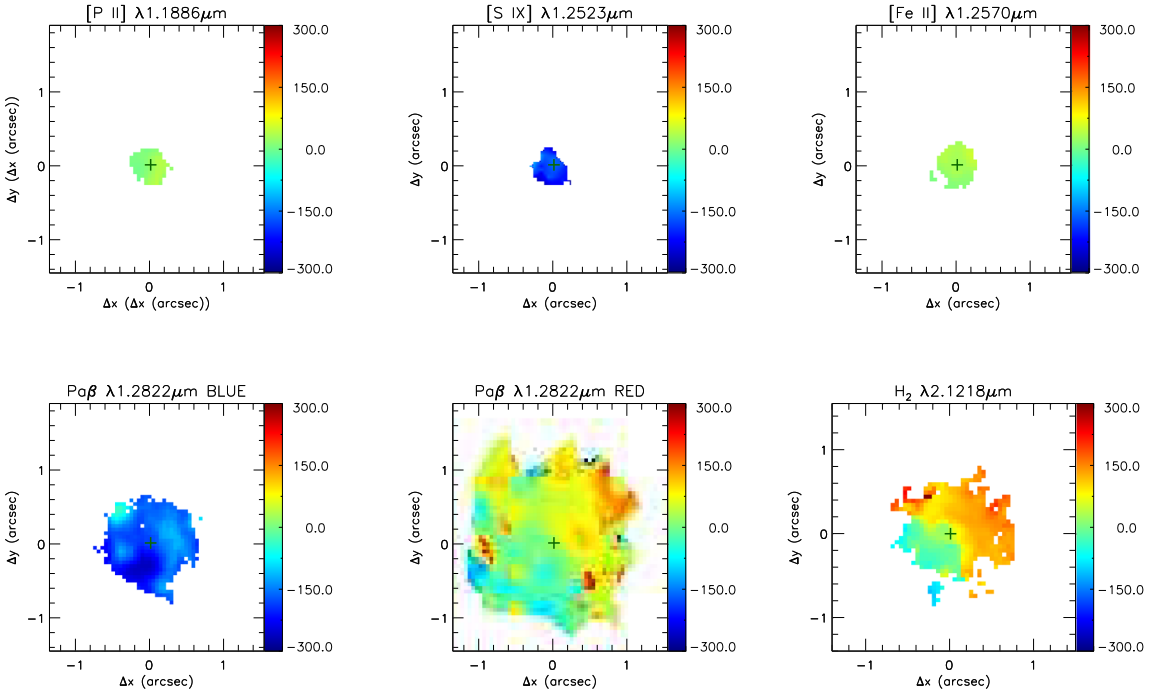

Figure 5. Centroid velocity fields for the [P II]λ1.1886 μm (top-left), [S IX]λ1.2523 μm (top-middle), [Fe II]λ1.2570 μm components (top-right), Pa β blue component (bottom-left), Pa β red component (bottom-middle), $H_2\lambda$2.1218 μm (bottom-right). The central cross marks the position of the nucleus. The colour bars show the velocities in units of km s^{-1}.

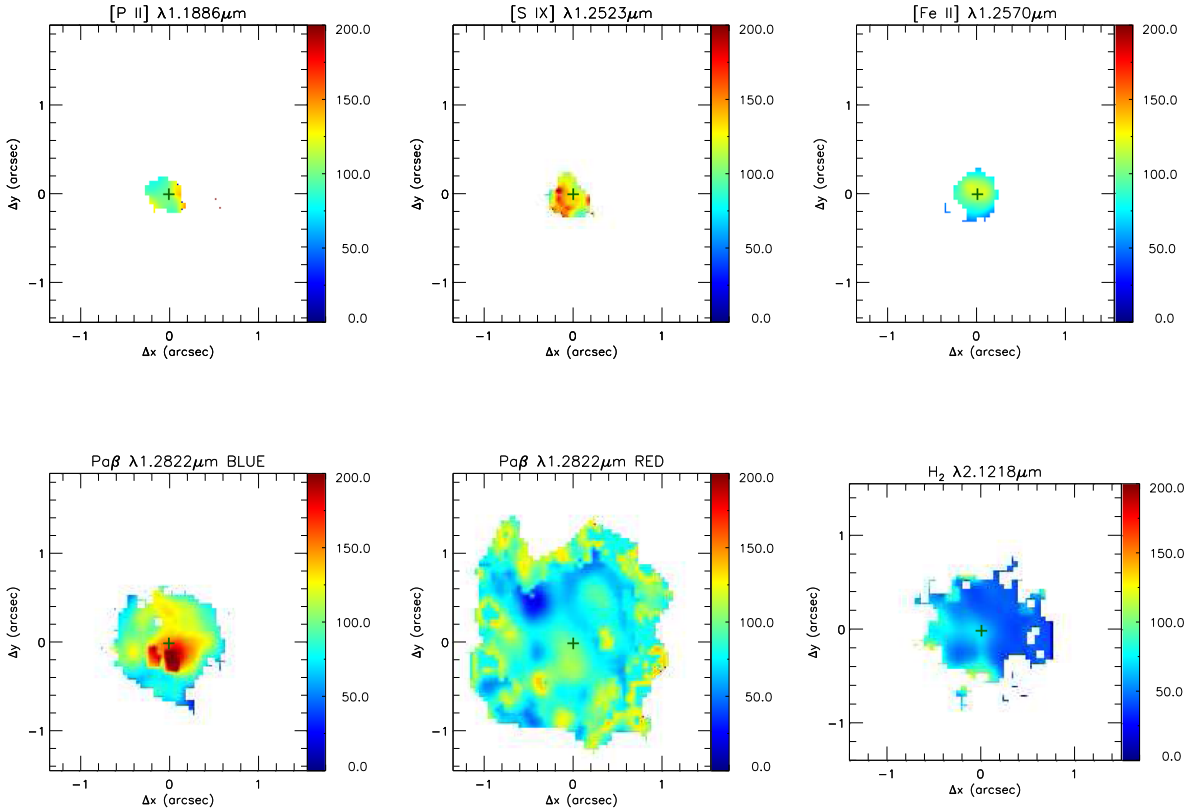

Figure 6. σ maps for the same emission lines of Fig. 5. The central cross marks the position of the nucleus. The colour bars show the σ values in units of km s^{-1}.

velocity v_*. For the NIR the values of σ_* cannot be derived with precision due the low spectral resolution of the EPS models, ergo, we do not use them. By minimizing the following equation we get the final fit

$$\chi^2 = \sum_{\lambda} [(O_\lambda - M_\lambda)\omega_\lambda]^2, \quad (2)$$

with spurious features and emission lines being excluded from the fit by fixing $\omega_\lambda = 0$.

The best fit for the observed spectrum should have the ideal base set of SSPs, since it should cover the range of spectral properties observed in the galaxy sample (Cid Fernandes et al. 2005) and provide enough resolution in age and metalicity. A library of integrated spectra of star clusters is a good base set, since they depend only on ages and metallicities of the stars being free from any assumptions on stellar evolution and initial mass function (Bica & Alloin 1986; Riffel et al. 2011a). So far, though, there is no such library available in the literature for the NIR spectral region. To get around this problem, we used the base set of theoretical SSPs covering this spectral region of Maraston (2005). The NIR carries fingerprints from evolved stars (Riffel et al. 2007; Ramos Almeida, Pérez García & Acosta-Pulido 2009; Martins et al. 2013) and these are crucial to model the absorption line spectra of the galaxies. They include empirical spectra of C- and O-rich stars and thus, are able to predict these features. The base comprises SSP synthetic spectra covering ages from 1 to 15 Gyr according to a grid of 67 models with four metallicities. The final base set comprises 31 ages, $t = 0.0010$, 0.0030, 0.0035, 0.0040, 0.0050, 0.0055, 0.0060, 0.0065, 0.0070, 0.0075, 0.0080, 0.0085, 0.0090, 0.010, 0.015, 0.020, 0.025, 0.030, 0.050, 0.080, 0.2, 0.3, 0.4, 0.5, 0.7, 0.8, 1,1.5, 2, 3, and 13 Gyr, and four metallicities, $Z = 0.02$, 0.5, 1, and 2 $Z_\odot$, with a final set of 124 SSPs.

We also included blackbody functions for temperatures in the range of 700–1400 K in steps of 100 K (Riffel et al. 2009b) and a power law ($F_\nu \propto \nu^{-1.5}$) in order to account for possible blackbody contributions from dust emission (BB) and from featureless continuum (FC), respectively, at the nucleus.

The resulting maps for the spectral synthesis are shown in Figs 8 and 9. Following Riffel et al. (2010b), we have binned the contribution of the SSPs into a reduced population vector with only three components that we call SPC (stellar population component) comprising three age ranges: young (x_y, $t \leq 50$ Myr); intermediate (x_i, 50 Myr $< t \leq 2$ Gyr) and old (x_o, 2 Gyr $< t \leq 15$ Gyr). In Fig. 8, we show the spatial distribution of the per cent flux contribution of each stellar component at 2.12 μm. In the top panels, we show the light-fraction of the SPC contributions and in the bottom panel the mass fraction contributions. Regarding the BB components, shown in Fig. 9 we have grouped them into a cold (BB$_c$, $700 < T < 1000$) and hot (BB$_h$, $1000 < T < 1400$) component.

The old SP flux contribution x_o dominates in a ring of radius ≈0.6 arcsec (230 pc), and in mass the ring extends inwards down to 0.3 arcsec (115 pc) from the nucleus, except for a small region to the east-southeast (E-SE) where the intermediate age component dominates. The largest contribution of the intermediate age SP x_i in light is observed between 0.3 arcsec (115 pc) and 0.5 arcsec (190 pc) and ranges from 40 to 100 per cent, the maximum contribution observed to the E-SE, where it also dominates the contribution in mass, as pointed out above. There is just a small contribution of young SP in light beyond the ring of old SP and around the nucleus (within 0.3 arcsec/115 pc).

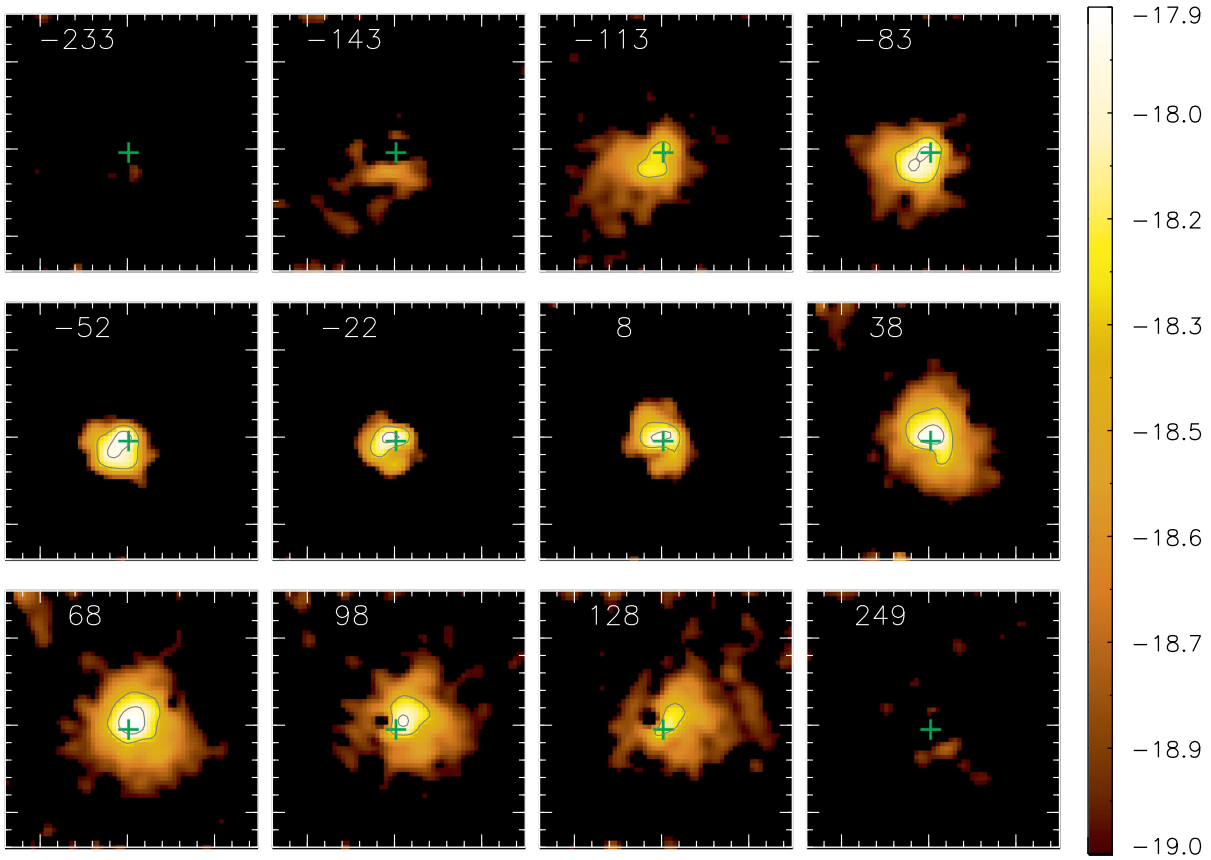

Figure 7. Channel maps along the H_2 emission-line profile, centred at the velocity shown in the upper-left corner of each panel in km s^{-1}. The cross marks the position of the nucleus.

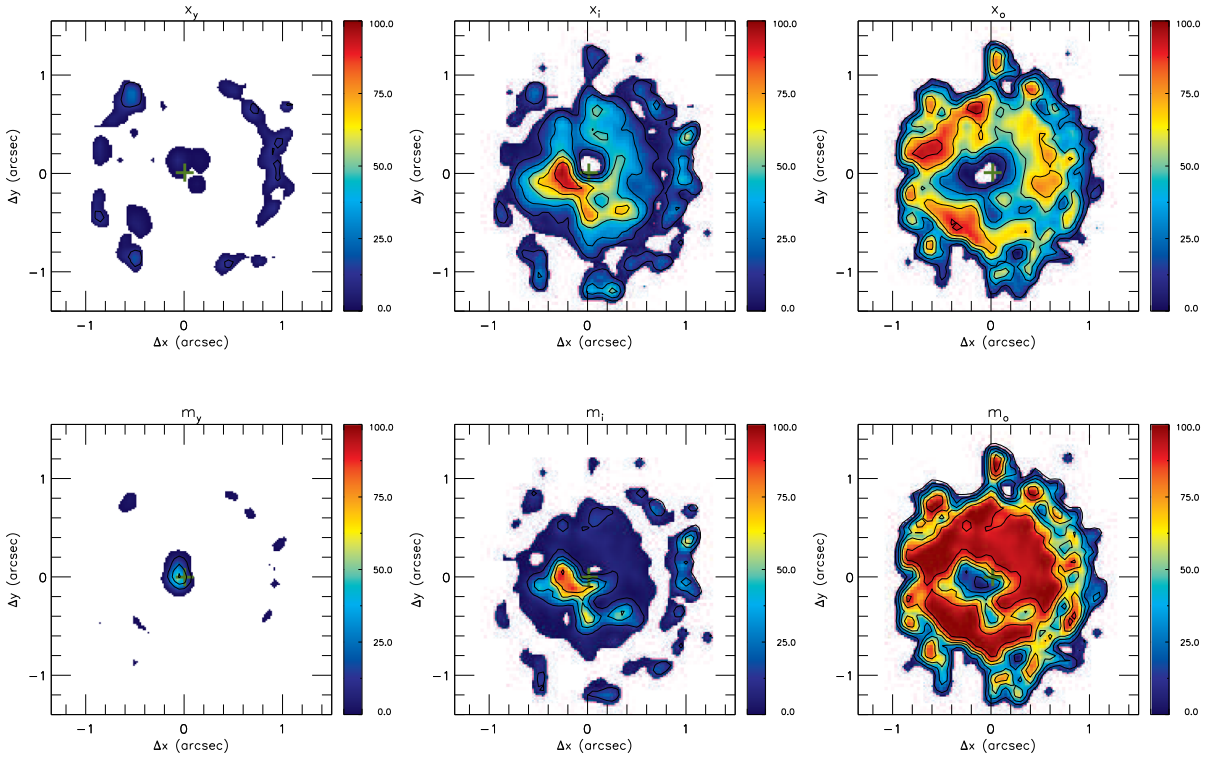

Figure 8. Spatial distributions of the per cent contribution of each SPC to the flux at $\lambda = 2.12$ μm (x_j) (top panels) and to the mass (m_j) (bottom panels), where j represents the age of the SPC: young ($t \leq 50$ Myr); intermediate (50 Myr $< t \leq 2$ Gyr) and old (2 Gyr $< t \leq 15$ Gyr).

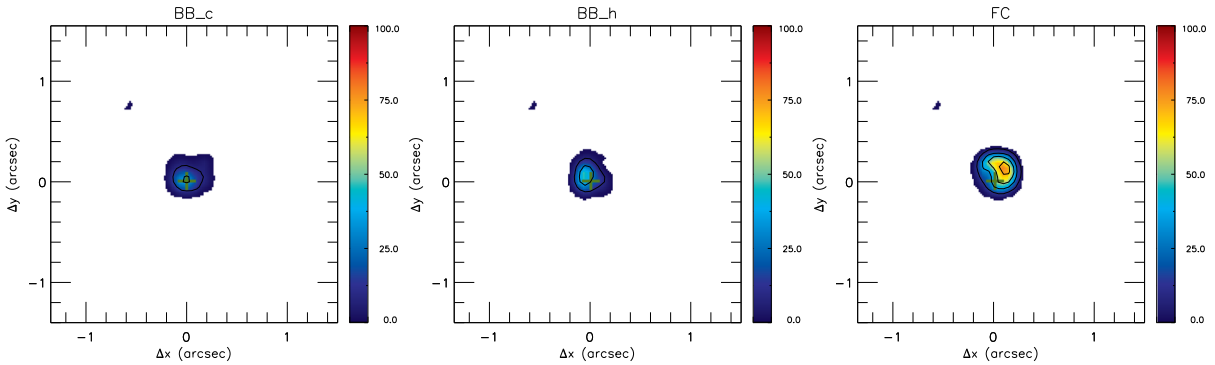

Figure 9. From left to right: spatial distribution of the cold dust emission (BB_c, 0 K < T < 1000 K); the hot dust emission (BB_h, 1000 K < T < 1400 K) and of the featureless continuum, FC.

In Fig. 9, we show the contributions of the BB and FC components. They are observed only at the nucleus and are essentially unresolved, with contributions reaching up to 20 per cent (±10 per cent) for both the hot (BB_h) and cold (BB_c) components and reaching up to 80 per cent (±10 per cent) for the FC.

4 DISCUSSION

4.1 Flux distributions and masses of ionized and molecular gas

The flux distribution is only barely resolved for [P II], [S IX], and [Fe II] emission lines, being more extended for Pa β and H_2, where it reaches 500 pc and 230 pc, respectively, from the nucleus, for a limiting S/N ratio ≈3. We have used the latter two to calculate the masses of the ionized and molecular gas within the inner 1×1 kpc.

The mass of ionized gas in the inner 1×1 kpc of the galaxy can be estimated using (e.g. Scoville et al. 1982; Riffel et al. 2008; Storchi-Bergmann et al. 2009; Schönell et al. 2014)

$$M_{\rm H\,II} \approx 5.1 \times 10^{16} \left(\frac{F_{\rm Pa\,\beta}}{\rm erg\,s^{-1}cm^{-2}}\right) \left(\frac{D}{\rm Mpc}\right)^2 [{\rm M}_\odot], \quad (3)$$

where, $F_{\rm Pa\,\beta}$ is the integrated flux for the Pa β emission line and D is the distance to NGC 5548. We have assumed an electron temperature $T = 10^4$ K and electron density $N_e = 100\,{\rm cm}^{-3}$ (Osterbrock & Ferland 2006).

The mass of warm molecular gas can be obtained using (Scoville et al. 1982)

$$M_{\rm H_2} \approx 5.0776 \times 10^{13} \left(\frac{F_{\rm H_2\lambda2.1218}}{\rm erg\,s^{-1}cm^{-2}}\right) \left(\frac{D}{\rm Mpc}\right)^2 [{\rm M}_\odot], \quad (4)$$

where $F_{\rm H_2\lambda2.1218}$ is the integrated flux for the $H_2\lambda2.1218$ μm emission line and we have used the vibrational temperature $T = 2000$ K (Riffel et al. 2008, 2010b; Storchi-Bergmann et al. 2009; Schönell et al. 2014).

Integrating over the whole IFU field, we obtain the following values for the masses: $M_{\rm H\,II} = 4.8\pm0.6 \times 10^6$ $M_\odot$ and $M_{\rm H_2} = 1.1\pm0.2 \times 10^3$ $M_\odot$, which are similar to those we have obtained in previous studies for other Seyfert galaxies, which are in the range 0.1×10^6 $M_\odot \leq M_{\rm H\,II} \leq 1.7 \times 10^6$ $M_\odot$ (Riffel et al. 2010a; Diniz et al. 2015) and 66 $M_\odot \leq M_{\rm H_2} \leq 3300$ $M_\odot$ (Riffel et al. 2008, 2010a), respectively.

The mass of molecular gas is thus 10^3 times smaller than that of the ionized gas but, as discussed in Storchi-Bergmann et al. (2009), this H_2 mass represents only that of warm gas emitting in the NIR. The total mass of molecular gas is dominated by the cold gas, and the usual proxy to estimate the cold H_2 mass has been the CO emission. A number of studies have derived the ratio between the cold and warm H_2 gas masses by comparing the masses obtained using the CO and NIR emission. Dale et al. (2005) obtained ratios in the range 10^5–10^7; using a larger sample of 16 luminous and ultraluminous infrared galaxies, Müller-Sánchez et al. (2006) derived a ratio $M_{\rm cold}/M_{\rm warm} = 1$–$5\times 10^6$. More recently, Mazzalay et al. (2013) compiled from the literature values of $M_{\rm cold}$ derived from CO observations and H_2 2.12 μm luminosities for a larger number of galaxies, covering a wider range of luminosities, morphological, and nuclear activity types. From that, an estimate of the cold H_2 gas mass can be obtained from

$$M_{\rm H_2\,cold} \approx 1174 \left(\frac{L_{\rm H_2\lambda2.1218}}{L_\odot}\right), \quad (5)$$

where $L_{\rm H_2\lambda2.1218}$ is the luminosity of the $H_2$2.12 μm line. The resulting mass value is $M_{\rm H_2\,cold} = 5.8\pm1.2 \times 10^8$ $M_\odot$.

In order to compare the masses obtained here with those of our previous studies of other galaxies, over different field-of-views, we have also calculated the mass surface density of the ionized and molecular gas distributions. Table 1 shows the integrated mass values, corresponding areas and resulting mass surface densities for NGC 5548 in comparison to those of previous studies by our group. Considering the extents of the flux distributions down to S/N ≈3, the surface densities in ionized and total (warm + cold) molecular gas in NGC 5548 are 7.2±0.8 and 3473±700 $M_\odot$ pc^{-2}, respectively. These values agree with those found in our previous studies, which range from 1.4 to 125 $M_\odot$ pc^{-2} for the mass surface density of ionized gas and 384 to 9600 $M_\odot$ pc^{-2} for the mass surface density of molecular gas as we can see in Table 1.

4.2 Gaseous kinematics

In Fig. 5 we show the centroid velocity fields of the observed emission lines, where the [P II]λ1.1886 μm and [Fe II]λ1.125 70 μm compact (barely resolved) velocity fields show values close to zero, while the [SIX]λ1.2523 μm velocity field is also compact but is all blueshifted to ≈−300 km s^{-1}. The velocity field of Pa β is more extended showing two components: one is all blueshifted, up to −400 km s^{-1}, and the other one shows a rotation pattern, similar to the velocity field observed also for H_2, which will be discussed in the following section.

4.2.1 *Rotation velocity model*

A rotation pattern is observed both for the Pa β red component and H_2 velocity fields (Fig. 5), but that for H_2 is more regular, and the

Table 1. Areas, masses (M) and mass surface densities (μ) for NGC 5548 and previous studied galaxies. The estimated errors are of the order of 20 per cent in the fluxes, and this propagates to the masses and surface mass densities. References: 1 – This work; 2 – Riffel & Storchi-Bergmann (2011); 3 – Riffel et al. (2014); 4 – Riffel et al. (2010a); 5 – Diniz et al. (2015); 6 – Riffel, Storchi-Bergmann & Winge (2013); 7 – Riffel et al. (2008); 8 – Storchi-Bergmann et al. (2009); 9 – Schönell et al. (2014); 10 – Riffel, Storchi-Bergmann & Riffel (2015).

Galaxies	Area (H_2)	Area (H II)	M $(H_2)_h$	M $(H_2)_c$	M (H II)	μ $(H_2)_h$	μ $(H_2)_c$	μ (H II)	Ref.
NGC 5548	1.7×10^5	6.7×10^5	2.3×10^2	1.7×10^8	2.2×10^6	6.6×10^{-3}	3473	7.2	1
Mrk 1157	2.8×10^5	1.8×10^5	2.3×10^3	1.6×10^9	5.4×10^6	8.2×10^{-3}	5714	45	2
NGC 1068	3.8×10^4	1.5×10^4	29	2×10^7	2.2×10^4	7.6×10^{-4}	526	1.5	3
Mrk 1066	2.5×10^5	1.9×10^5	3.3×10^3	2.4×10^9	1.7×10^7	1.3×10^{-2}	9600	89	4
NGC 2110	1.1×10^5	7×10^4	1.4×10^3	9.9×10^8	1.7×10^6	1.3×10^{-2}	9000	24	5
Mrk 79	9.8×10^5	7.8×10^5	3×10^3	2.2×10^9	7×10^6	3.1×10^{-3}	2245	9	6
NGC 4051	1.3×10^4	1.4×10^4	66	4.7×10^7	1.4×10^5	5.3×10^{-3}	3760	9.8	7
NGC 4151	2.4×10^4	1.9×10^4	240	1.7×10^8	2.4×10^6	1.8×10^{-2}	7083	125	8
Mrk 766	3×10^5	2.7×10^5	1.3×10^3	9.8×10^8	7.6×10^6	4.3×10^{-3}	3266	28	9
NGC 5929	1.2×10^5	7×10^4	471	3.5×10^8	1.3×10^6	3.9×10^{-3}	2966	18	10

Note. All mass (M) units are in $M_\odot$, area units in pc^2 and the mass surface densities (μ) in $M_\odot\ pc^{-2}$.

corresponding velocity dispersions are also lower, supporting that the H_2 is more confined to the galaxy plane (as we have observed also in previous studies of other galaxies). Aiming to obtain parameters such as the systemic velocity, orientation of the line of the nodes and the inclination of the disc, we fitted a rotation model for the H_2 centroid velocity field assuming that the emitting gas is rotating in a central potential (Barbosa et al. 2006). For this kinematic model (van der kruit & Allen 1978; Bertola et al. 1991), it is assumed that the gas has circular orbits in a plane, and the velocity field is given by

$$V_{\rm mod}(R, \Psi) = V_{\rm sys} + \frac{A R \cos(\Psi - \Psi_0) \sin\theta \cos^p\theta}{(R^2)(\sin^2(\Psi - \Psi_0) + \cos^2\theta \cos^2(\Psi - \Psi_0) + c_0^2 \cos^2\theta)^{p/2}}, \quad (6)$$

where $v_{\rm sys}$ is the systemic velocity, A is the centroid velocity amplitude, Ψ_0 is the major axis position angle, c_0 is a concentration parameter, θ is the angle between the disc plane and the sky plane, p is a model fitting parameter (which is ≈1 for infinite masses in a Plummer potential) and R and Ψ are the coordinates of each pixel in the plane of the sky.

In the fit, the location of the kinematical centre was not allowed to vary, being fixed to the position of the peak of the continuum, adopted to be the nucleus of the galaxy. In Fig. 10 we show the centroid velocity field of H_2 in the top-left panel, the resulting model from the fit in the top-right panel and residual maps (centroid velocity field of the emitting gas – model) in the bottom panels. The resulting parameters of the fit are: $v_{\rm sys} = 5160 \pm 52$ km s^{-1}, which is close to the systemic velocity reported in De Vaucouleurs et al. (1991) that is 5149 km s^{-1}, $\Psi_0 = 126^\circ$ being 16° higher than the one quoted in NED (Nasa Extragalactic Database), from a large-scale continuum image. The H_2 discs – observed within the inner 400 pc – thus seems to follow the orientation of the large scale disc. The fit also gives an inclination for the disc relative to the plane of the sky of $\theta = 10^\circ$. The best model shows a compact velocity curve, peaking at only ≈200 pc from the nucleus. We have found similarly steep velocity curves for H_2 in our previous studies of active galaxies (Riffel & Storchi-Bergmann 2011; Schönell et al. 2014). Although this velocity field seems not very well constrained in the outer parts (due to the limited coverage of the H_2 velocity field), the residual map for H_2 shows that at most locations the deviations from the model are smaller than ≈40 km s^{-1}. The residuals for the Pa β velocity field are larger, and could be due to the presence of other components and/or a less steep velocity field for this line as we found also in our previous studies of other galaxies.

4.2.2 *Mass outflow rate*

The blueshift observed in the Pa β emission line can be interpreted as due to an outflow and can be used to estimate the gas mass outflow rate. We have assumed a conical geometry in which we considered a possible range for the height (h) of the cone between 1.0 arcsec (384 pc) to 2.0 arcsec (768 pc) – under the assumption that the height of the cone is of the order of the diameter of its base, as we cannot observe this height.

With this range of heights we have the resulting opening angles of ≈27°.5, and ≈53°. The outflow is thus calculated at a distance from the nucleus of 1.0 arcsec and 2.0 arcsec, through a circular area of radius $r = 0.5$ arcsec estimated from Fig. 5. The mass outflow rate can then be estimated by

$$\dot{M}_{\rm out} = m_{\rm p}\, N_{\rm e}\, v\, f\, A \quad (7)$$

and the filling factor (f) can be obtained from

$$f = \frac{L_{\rm Pa\,\beta}}{j_{\rm Pa\,\beta}\, V}, \quad (8)$$

where $m_{\rm p}$ is the proton mass, $N_{\rm e}$ the electron density, v is velocity of the outflowing gas and $L_{\rm Pa\,\beta}$ and $j_{\rm Pa\,\beta}$ are the luminosity and the emission coefficient of Pa β, respectively (Riffel et al. 2011b; Schönell et al. 2014), and the volume of the outflowing region is $v = A \times (h/3)$.

We have assumed that $N_{\rm e} = 500$ cm^{-3} and measured $L_{\rm Pa\,\beta} = 3.89 \pm 0.43 \times 10^{39}$ erg s^{-1}, for $j_{\rm Pa\,\beta} = 4.07 \times 10^{-22}$ erg cm^{-3} s^{-1} (Osterbrock & Ferland 2006) and $v_{\rm out} = 280$ km s^{-1}. The value for the velocity of the outflow ($v = 280$ km s^{-1}) was obtained as the average velocity of the blueshifted component of Pa β. With the geometry described above we obtain $\dot{M}_{\rm out} = 9 \pm 1\ M_\odot\ {\rm yr}^{-1}$ for $h = 1.0$ arcsec and $\dot{M}_{\rm out} = 4.5 \pm 0.5\ M_\odot\ {\rm yr}^{-1}$ for $h = 2.0$ arcsec. The values found here for $\dot{M}_{\rm out}$ are somewhat larger than those we have found in our previous studies of other Seyfert galaxies but are in good agreement with those found in Veilleux et al. (2005) for outflows observed in other active galaxies, which range from 0.1 to 10 $M_\odot\ {\rm yr}^{-1}$, as well as with those found by Müller-Sánchez et al. (2011), which range from 2.5 to 120 $M_\odot\ {\rm yr}^{-1}$.

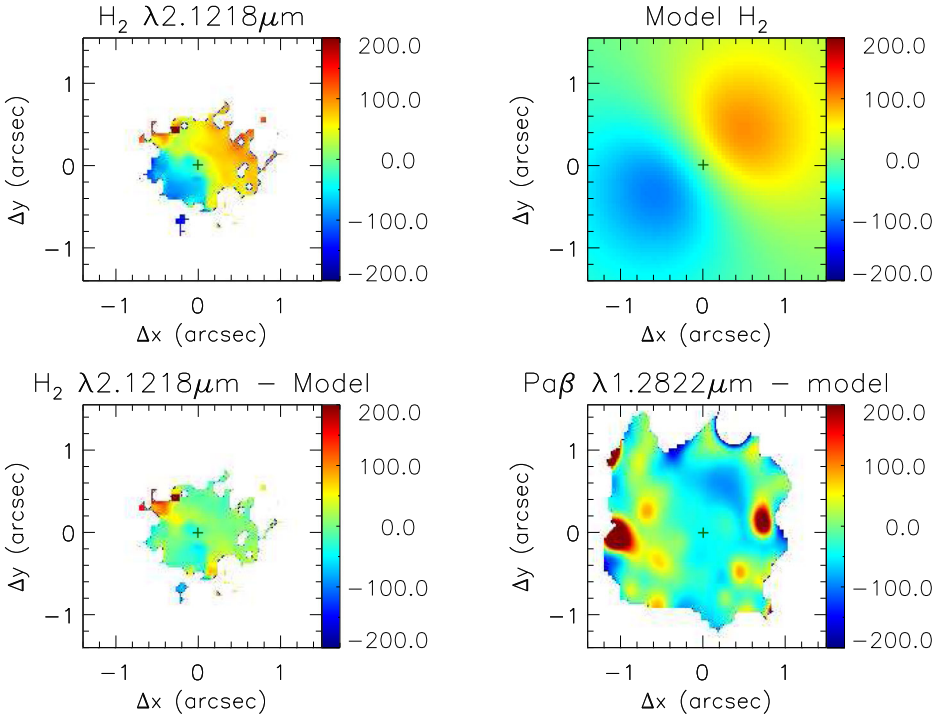

Figure 10. Top panels: H_2 velocity field and fitted rotating disc model; bottom panels: residual maps between the observed velocity fields of H_2 and Pa β and the model.

To estimate the kinetic power of the outflow we can use the following relation (Storchi-Bergmann et al. 2010; Schönell et al. 2014):

$$\dot{E} \approx \frac{\dot{M}_{\rm out}}{2}(v^2 + \sigma^2), \quad (9)$$

where v is the velocity of the outflowing gas and σ is its velocity dispersion. Using $\sigma \approx 130$ km s^{-1} and $v = 280$ km s^{-1}, we obtain $\dot{E} \approx 2.1 \times 10^{41}$ erg s^{-1}. The value found for $\dot{E}$ is in good agreement with those found for Seyfert galaxies and compact radio sources (Morganti, Tadhunter & Oosterloo 2005). This value is similar to that obtained for Mrk 1157 (Riffel & Storchi-Bergmann 2011), of $\dot{E} \approx 5.7 \times 10^{41}$ erg s^{-1} and for Mrk 766 (Schönell et al. 2014), of $\dot{E} \approx 2.9 \times 10^{41}$ erg s^{-1}, it is also within the range of those found by Müller-Sánchez et al. (2011), between 0.6 and 50×10^{41} erg s^{-1}. To compare the $\dot{E}$ value with the bolometric luminosity, we estimate the latter as 10 times the X-ray luminosity of 5.1×10^{42} erg s^{-1} (Rivers, Markowitz & Rothschild 2011), resulting in $\dot{E} \approx 0.004\ L_{\rm Bol}$. This value is about the one quoted in galaxy evolution simulations by Di Matteo, Springel & Hernquist (2005) and Hopkins & Elvis (2010) – 0.5 per cent $L_{\rm Bol}$ – as the necessary power of the outflow to have a significant impact on the evolution of the galaxy.

4.3 Stellar population

From the spectral synthesis we conclude that, at the unresolved nucleus (within ≈0.2 arcsec), the main components contributing to the continuum flux in the NIR are the featureless contribution from the AGN (≈70 per cent) followed by the blackbody components – 20 per cent for both the hot (BB_h) and cold (BB_c) that can be attributed to the dusty torus. Some minor contribution in flux from the young stellar component (≈10 per cent) was also found there.

Moving outwards, in a ring extending from 0.2 arcsec (80 pc) to 0.5 arcsec (190 pc) there is a ≈50 per cent contribution in flux from the intermediate age component that increases to almost 100 per cent in flux and also in mass in a patch to the E-SE of the nucleus. The rest is contributed by the old component that dominates outward from the ring, both in flux and mass.

In general, our results for the SP synthesis are similar to those of our previous works (Riffel et al. 2011b; Storchi-Bergmann et al. 2012) in other Seyfert galaxies, where we have found 100–300 pc circumnuclear rings with increased contribution of young to intermediate age SP.

Results from other authors also support the presence of young to intermediate age stellar populations in circumnuclear rings around AGN. In Davies et al. (2007), for example, the authors investigated the star formation history in the circumnuclear region of a sample of nine Seyfert galaxies using the SINFONI NIR integral field spectrograph with adaptive optics at the Very Large Telescope. With measurements of the Br γ emission-line equivalent widths, supernova rates and mass-to-light ratios, they found circumnuclear discs of typical diameters of tens of pc with a 'characteristic' age in the range 10–300 Myr, corresponding closely to our 'intermediate' age range, therefore agreeing with our results.

5 CONCLUSIONS

We have mapped the gas flux distribution, excitation, and kinematics as well as the SP from the inner ≈500 pc radius of the Seyfert 1 galaxy NGC 5548 using NIR *J*- and *K*-band integral field spectroscopy. The conclusions of this work are listed below.

(i) The emission-line flux distributions of [P II], [S IX], and [Fe II] are barely resolved, extending to ≈150 pc from the nucleus.

(ii) The emission-line flux distributions of Pa β and H_2 are more extended, reaching up to ≈450 pc and ≈300 pc from the nucleus, respectively, observed only in blueshift, at ≈300 km s^{-1}, as due to an outflow approximately perpendicular to the plane of the sky.

(iii) The Pa β emission line has a second component observed in blueshift within ≈300 pc from the nucleus, with velocities ranging from −100 to −400 km s^{-1}. The [S IX] emission is observed only in blueshift , at ≈−300 km s^{-1}. These components have been interpreted as due to an outflow oriented approximately perpendicularly to the plane of the sky.

(iv) The mass outflow rate in ionized gas is estimated to be ≈6.8±0.75 M$_\odot$ yr^{-1}.

(v) The power of the outflow is 0.4 per cent $L_{\rm Bol}$, which is of the order of the minimum necessary to significantly influence (by pushing gas out of the galaxy) the evolution of the galaxy.

(vi) The velocity fields of H_2 and the red component of Pa β show a rotation pattern.

(vii) Fitting a rotation model to the H_2 velocity field, we derived a systemic velocity for the galaxy of 5160±52 km s^{-1}.

(viii) The mass of ionized gas is $M_{\rm H\,II} = 4.8\pm0.6 \times 10^6$ M$_\odot$;

(ix) The mass of the hot molecular gas is $M_{\rm H_2} = 1.1\pm0.2 \times 10^3$ M$_\odot$ and the estimated cold molecular gas mass is $M_{\rm H_2} = 5.8\pm1.2 \times 10^8$ M$_\odot$.

(x) The surface densities in ionized and cold molecular gas are 7.2±0.8 and 3473±700 M$_\odot$ pc^{-2}, respectively.

(xi) Spectral synthesis of the continuum reveals that, at the nucleus, a featureless power-law continuum dominates the flux, with some contribution from blackbody components attributed to a dusty torus and a minor contribution from a young SP.

(xii) Outwards from the nucleus, an intermediate age component contributes with ≈40 per cent in flux in a ring extending from 0.2 arcsec (80 pc) to 0.5 arcsec (190 pc) with an increased contribution in a patch to the E-SE that reaches almost 100 per cent both in flux and in mass, while the remainder contribution is attributed to the old component that dominates also outwards.

ACKNOWLEDGEMENTS

We thank an anonymous referee for useful suggestions which helped to improve the paper. This work is based on observations obtained at the Gemini Observatory, which is operated by the Association of Universities for Research in Astronomy, Inc., under a cooperative agreement with the NSF on behalf of the Gemini partnership: the National Science Foundation (United States), the Science and Technology Facilities Council (United Kingdom), the National Research Council (Canada), CONICYT (Chile), the Australian Research Council (Australia), Ministério da Ciência e Tecnologia (Brazil) and southeastCYT (Argentina). This research has made use of the NASA/IPAC Extragalactic Database (NED) which is operated by the Jet Propulsion Laboratory, California Institute of Technology, under contract with the National Aeronautics and Space Administration. This work has been partially supported by the Brazilian institution CNPq.

REFERENCES

Asari N. V., Cid Fernandes R., Stasínska G., Torres-Papaqui J. P., Mateus A., Sodré L., Schoenell W., Gomes J. M., 2007, MNRAS, 381, 263
Barbosa F. K. B., Storchi-Bergmann T., Cid Fernandes R., Winge C., Schmitt H., 2006, MNRAS, 371, 170
Barillard A. et al., 2011, A&A, 532, 74
Bertola F., Bettoni D., Danziger J., Sadler E., Sparke L., de Zeeuw T., 1991, ApJ, 373, 369
Bica E., Alloin D., 1986, A&A, 162, 21
Cardelli J. A., Clayton G. C., Mathis J. S., 1989, ApJ, 345, 245
Cid Fernandes R., Gu Q., Melnick J., Terlevich E., Terlevich R., Kunth D., Rodrigues Lacerda R., Joguet B., 2004, MNRAS, 355, 273
Cid Fernandes R., Mateus A., Sodré Laerte, Stasínska G., Gomes J. M., 2005, MNRAS, 358, 363
Cid Fernandes R. et al., 2009, Rev. Mex. Astron. Astrofis. Ser. Conf., 35, 127
Crenshaw D. M., Kraemer S. B., 2007, ApJ, 659, 250
Crenshaw D. M., Kraemer S. B., Schmitt H. R., Kaastra J. S., Arav N., Gabel J. R., Korista K. T., 2009, ApJ, 698, 281
Crenshaw D. M., Schmitt H. R., Kraemer S. B., Mushotsky R. F., Dunn J. P., 2010, ApJ, 708, 419
Dale D. A., Sheth K., Helou G., Regan M. W., Hüttemeister S., 2005, AJ, 129, 2197
Davies R. I., Sánchez F. M., Genzel R., Tacconi L. J., Hicks E. K. S., Friedrich S., Sternberg A., 2007, ApJ, 671, 1388
Davies R. I. et al., 2014, ApJ, 792, 101
Davies R. I., Maciejewski W., Hicks E. K. S., Tacconi L. J., Genzel R., Engel H., 2009, ApJ, 702, 114
de Vaucouleurs G., de Vaucouleurs A., Corwin H. G. Jr Buta R. J., Paturel G., Fouqué P., 1991, Third Reference Catalogue of Bright Galaxies. Springer, New York
Di Matteo T., Springel V., Hernquist L., 2005, Nature, 433, 604
Diniz M. R., Riffel R. A., Storchi-Bergmann T., Winge C., 2015, MNRAS, 453, 1727
Fathi K., Storchi-Bergmann T., Riffel R. A., Winge C., Axon D. J., Robinson A., Capetti A., Marconi A., 2006, ApJ, 641, L25
Ferruit P., Wilson A. S., Mulchaey J., 2000, ApJS, 128, 139
Fischer T. C., Crenshaw D. M., Kraemer S. B., Schmitt H. R., Mushotsky R. F., Ward M. J., 1993, ApJ, 727, 71
Fischer T. C., Crenshaw D. M., Kraemer S. B., Schmitt H. R., Trippe M. L., 2010, AJ, 140, 577
Holt J., Tadhunter C., Morganti R., Bellamy M., González Delgado R. M., Tzioumis A., Inskip K. J., 2006, MNRAS, 370, 1633
Hopkins P. F., Elvis M., 2010, MNRAS, 401, 7
McGregor P. J. et al., 2003, in Iye M., Moorwood A. F. M., eds, Proc. SPIE Conf. Ser. Vol. 4841, Instrument Design and Performance for Optical/Infrared Ground-based Telescopes. SPIE, Bellingham, p. 1581
Malkan M. A., Gorjian V., Tam R., 1998, ApJS, 117, 25
Maraston C., 2005, MNRAS, 362, 799
Martins L. P., Rodríguez-Ardila A., Diniz S., Riffel R., de Souza R., 2013, MNRAS, 435, 2861
Mateus A., Sodré L., Cid Fernandes R., Stasínska G., Schoenell W., Gomes J. M., 2006, MNRAS, 370, 721
Mazzalay X., Rodríguez-Ardila A., Komossa S., 2010, MNRAS, 405, 1315
Mazzalay X. et al., 2013, MNRAS, 428, 2389
Morganti R., Tadhunter C. N., Oosterloo T. A., 2005, A&A, L9, L13
Müller-Sánchez F., Davies R. I., Eisenhauer F., Tacconi L. J., Genzel R., Sternberg A., 2006, A&A, 454, 492
Müller Sánchez F., Davies R. I., Genzel R., Tacconi L. J., Eisenhauer F., Hicks E. K. S., Friedrich S., Sternberg A., 2009, ApJ, 691, 749
Müller-Sánchez F., Prieto M. A., Hicks E. K. S., Vives-Arias H., Davies R. I., Malkan M., Tacconi L. J., Genzel R., 2011, ApJ., 739, 69
Osterbrock D. E., Ferland G. J., 2006, Astrophysics of Gaseous Nebulae and Active Galactic Nuclei, 2nd edn. University Science Books, Mill Valley, CA
Ramos Almeida C., Pérez García A. M., Acosta-Pulido J. A., 2009, ApJ, 694, 1379
Riffel R. A., 2010, Ap&SS, 327, 239
Riffel R. A., Storchi-Bergmann T., 2011, MNRAS, 411, 469
Riffel R. A., Sorchi-Bergmann T., Winge C., Barbosa F. K. B., 2006, MNRAS, 373, 2
Riffel R., Pastoriza M. G., Rodríguez-Ardila A., Maraston C., 2007, ApJ, 659, 103
Riffel R. A., Storchi-Bergmann T., Winge C., McGregor P. J., Beck T., Schmitt H., 2008, MNRAS, 385, 1129
Riffel R. A., Storchi-Bergmann T., Dors O. L., Winge C., 2009a, MNRAS, 393, 783
Riffel R., Pastoriza M. G., Rodríıguez-Ardila A., Bonatto C., 2009b, MNRAS, 400, 273
Riffel R. A., Storchi-Bergmann T., Nagar N. M., 2010a, MNRAS, 404, 166

Riffel R. A., Storchi-Bergmann T., Riffel R., Pastoriza M. G., 2010b, ApJ, 713, 469
Riffel R., Ruschel-Dutra D., Pastoriza M. G., Rodríguez-Ardila A., Santos J. F. C., Jr, Bonatto C. J., Ducati J. R., 2011a, MNRAS, 410, 2714
Riffel R., Riffel R. A., Ferrari F., Storchi-Bergmann T., 2011b, MNRAS, 416, 493
Riffel R. A., Storchi-Bergmann T., Winge C., 2013, MNRAS, 430, 2249
Riffel R. A., Tibério V. B., Storchi-Bergmann T, McGregor P. J., 2014, MNRAS, 442, 656
Riffel R. A., Storchi-Bergmann T., Riffel R., 2015, MNRAS, 451, 3587
Riffel R. A. et al., 2016, MNRAS, 461, 4205
Rivers E., Markowitz A., Rothschild R., 2011, ApJS, 193, 3
Rodríguez-Ardila A., Prieto M. A., Viegas S., Gruenwald R., 2006, ApJ, 653, 1098
Schmitt H. R., Kinney A. L., 1996, ApJ, 463, 498
Schnorr Müller A., Storchi-Bergmann T., Riffel R. A., Ferrari F., Steiner J. E., Axon D. J., Robinson A., 2011, MNRAS, 413, 149
Schönell A. J. J., Riffel R. A., Storchi-Bergmann T., Winge C., 2014, MNRAS, 445, 427
Scoville N. Z., Hall D. N. B., Kleinmann S. G., Ridgway S. T., 1982, ApJ, 253, 136
Storchi-Bergmann T., Dors O., Jr, Riffel R. A., Fathi K., Axon D. J., Robinson A., 2007, ApJ, 670, 25
Storchi-Bergmann T., McGregor P., Riffel R., Rogemar A., Simões Lopes R., Beck T., Dopita M., 2009, MNRAS, 394, 1148
Storchi-Bergmann T., Simões Lopes R., McGregor P. Riffel, Rogemar A., Beck T., Martini P., 2010, MNRAS, 402, 819
Storchi-Bergmann T., Riffel R. A., Riffel R., Diniz M. R., Borges V. T., McGregor P. J., 2012, ApJ, 755, 87
van der Kruit P. C., Allen R. J., 1978, ARA&A, 16, 103
Veilleux S. A., Goodrich R. W., Hill G. J., 1997, ApJ, 477, 631
Veilleux S., Cecil G., Bland-Hawthorn J., 2005, ARA&A, 43, 769
Wilson A. S., Braatz J. A., Heckman T. M., Krolic J. H., Miley G. K., 1993, ApJ, 419, L61

This paper has been typeset from a TEX/LATEX file prepared by the author.